

# Micro-Air-Vehicle-Borne Near-Range SAR with Motion Compensation

Huaming Wu and Thomas Zwick

**Abstract**—The major difficulty of realizing a micro-air-vehicle-borne (MAV-borne) synthetic aperture radar (SAR) is the motion errors that need to be precisely measured and compensated. This paper presents two novel motion measuring algorithms specifically for near-range applications. These algorithms use only low-cost micro-electronic-mechanical system (MEMS) inertial measurement units (IMU). A MAV-borne SAR system was built equipped with a commercial off-the-shelf (COTS) motion sensing board. Several MAV-borne SAR measurements were performed for the first time in a hall with a realistic scene. SAR images were generated with proposed motion measuring algorithms in off-line mode. Obvious improvements in SAR image quality in terms of focusing have been observed after motion compensation with the proposed motion measuring algorithms. These results show that MAV-borne SAR together with low-cost IMU can yield very useful images.

## 1. INTRODUCTION

In the last decade, high-performance, compact, low-cost customized synthetic aperture radar (SAR) systems have been developed and equipped successfully on unmanned aerial vehicles (UAV) for remote sensing applications [1, 2]. On the other hand, there is also commercial short range radar available for micro air vehicles (MAV) as an altimeter [3] or for proximity warning [4]. In principle, by combining with SAR techniques, current commercial short range radar products can achieve very high azimuth resolution, and therefore additional applications are expected. For example, self-contained navigation system has been of particular interest for MAV applications in the cases where no GPS signals or no external cameras are available [5]. By using SAR technique, the on-board radar sensor is able to generate a high resolution image of the surrounding, which can be used to assist the current optical [6] or infrared camera [7] based systems.

Generally, the strapdown inertial navigation system (INS) used in remote sensing SAR applications for motion compensation consists of expensive high accuracy inertial measurement units (IMU) and requires external GPS signals to correct the accumulated bias. Therefore, it is not suitable for near-range civil applications, which are cost sensitive and sometimes work in in-door environments without GPS signals. Although low-cost strapdown INS based on micro-electronic-mechanical system (MEMS) devices has become more and more affordable for civil applications, it is not yet possible to build MEMS based INS which gives sub-meter position accuracy over one minute of operation without the aid of other sensors [8].

In Section 2, the procedure of SAR signal processing with a first-order motion compensation is briefly introduced. By exploiting the features of near-range SAR applications, two motion measuring algorithms using MEMS IMU are proposed in Section 3. In Section 4, the results of MAV-borne SAR measurements to verify these algorithms are presented.

---

*Received 20 December 2013, Accepted 7 February 2014, Scheduled 11 February 2014*

\* Corresponding author: Huaming Wu (huaming.w@gmail.com).

The authors are with the Institut fuer Hochfrequenztechnik und Elektronik, Karlsruhe Institute of Technology, Geb. 30.10, Kaiserstr 12, Karlsruhe 76128, Germany.

## 2. SAR PROCESSING WITH MOTION COMPENSATION

Considering the potential ultra-wide beamwidth used for the near-range SAR applications, the range migration algorithm (RMA), which is the most accurate frequency-domain SAR algorithm [9], is chosen at this initial step of research.

The dechirped raw intermediate frequency (IF) SAR data in azimuth-time ( $x_{\text{am}}$ ) range-frequency ( $k_r$ ) domain can be expressed as

$$\tilde{s}_{\text{IF}}(x_{\text{am}}, k_r) = s_{\text{IF}}(x_{\text{am}}, k_r) \cdot \exp(-jk_r \Delta r_t). \quad (1)$$

Here,  $s_{\text{IF}}(x_{\text{am}}, k_r)$  denotes the ideal IF data without motion errors, and  $\Delta r_t$  denotes the motion errors with regard to a certain target, which is composed of space-invariant motion errors,  $\Delta r_{\text{in}}$ , and space-variant motion errors,  $\Delta r_{\text{var}}$ .

For the ease of explanation, a constant deviation from the nominal trajectory in  $y$  axis in the 2D  $xy$ -plane and different components of the motion errors of a certain target  $t$  are illustrated in Figure 1. On the left side of Figure 1, the distance between the target and the radar's nominal position,  $r_t$ , is denoted by green color, while the real distance between the target and the radar's real position,  $\tilde{r}_t$ , is denoted by red color. The difference between  $\tilde{r}_t$  and  $r_t$  is the target's motion error,  $\Delta r_t$ , which is denoted by lilac color. As depicted on the right side of Figure 1,  $\Delta r_t$  can be decomposed into two components, i.e.,  $\Delta r_t = \Delta r_{\text{in}} + \Delta r_{\text{var}}$ . The space-invariant motion error,  $\Delta r_{\text{in}}$ , is the difference between the real trajectory and the nominal trajectory, which is denoted by the blue line. The space-variant motion error,  $\Delta r_{\text{var}}$ , is the residual part of  $\Delta r_t$ , which is denoted by the lilac dash line.

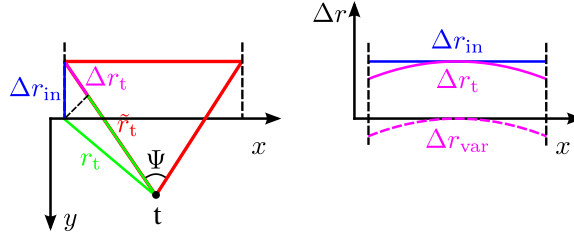


**Figure 1.** The relationship between  $\Delta r_t$ ,  $\Delta r_{\text{in}}$  and  $\Delta r_{\text{var}}$ .

Given the knowledge of  $\Delta r_{\text{in}}$ , an intuitive first-order motion compensation is applied to compensate the major part of motion errors in the raw IF data, which can be expressed as

$$\tilde{s}_{\text{IF},\text{in}}(x_{\text{am}}, k_r) = \tilde{s}_{\text{IF}}(x_{\text{am}}, k_r) \cdot \exp(jk_r \Delta r_{\text{in}}) = s_{\text{IF}}(x_{\text{am}}, k_r) \cdot \exp(-jk_r \Delta r_{\text{var}}). \quad (2)$$

This paper focuses on using low-cost IMU to measure the motion errors, so the space-variant motion errors,  $\Delta r_{\text{var}}$ , are assumed to be zero; a specific discussion about motion compensation for  $\Delta r_{\text{var}}$  can be found in [10]. Therefore, after performing the first-order motion compensation, the IF SAR data is assumed to be the error-free  $s_{\text{IF}}(x_{\text{am}}, k_r)$ .

## 3. MOTION MEASURING ALGORITHMS

In this paper, strapdown inertial measurement scheme is used, namely IMU devices are mounted directly onto the vehicle-radar rigid body to form a strapdown system [11]. The accelerometers measure the accelerations,  $a$ , in the 3 axes of the body frame and the gyroscopes measure the angular rates,  $\omega$ , about the 3 axes of the body frame. Both  $a$  and  $\omega$  are called degrees of freedom (DoF).

The geometry of SAR imaging and strapdown inertial navigation is illustrated in Figure 2. The SAR processing is performed in the Earth-fixed frame, while the antenna's coordinates in the Earth-fixed frame are calculated from measurements acquired by IMU in the body frame.

As shown in Figure 2,  $\tilde{r}_t$  and  $r_t$  are the real and the nominal slant range respectively, and the difference between them is the motion errors,  $\Delta r_t$ . The superscript “ $e$ ” denotes the measurements expressed in the Earth-fixed frame, while the superscript “ $b$ ” denotes the measurements expressed in the body frame. The image display plane (IDP) expressed in the Earth-fixed frame is specified by a

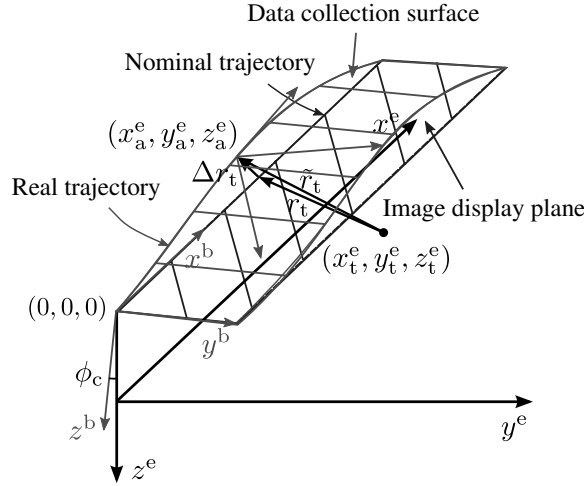


**Figure 2.** Geometry of SAR imaging and strapdown inertial navigation.

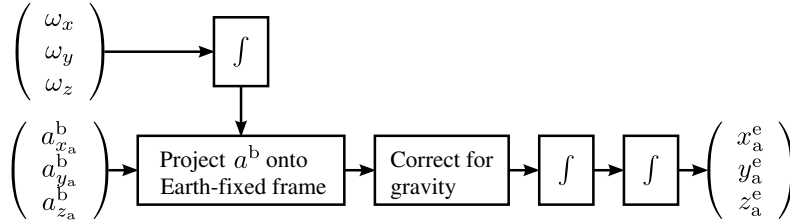


**Figure 3.** Procedure of strapdown inertial navigation algorithm.

constant roll angle  $\phi_c$  between the  $x^e y^e$ -plane and the IDP, which is determined by the configuration of the radar sensor. Data collection surface (DCS) is the instantaneous  $x^b y^b$ -plane expressed in the Earth-fixed frame.

The traditional strapdown inertial navigation algorithm is shown in Figure 3. It can be seen that 6 DoF are required to calculate the radar sensor’s position in the Earth-fixed frame. Assuming that targets are of the same height as the radar sensor for a short term in the near-range applications, only  $y_a^{\text{IDP}}$  is used to construct the compensation phase term,  $e^{jk_r \Delta r_{\text{in}}}$ , where  $\Delta r_{\text{in}} = -y_a^{\text{IDP}}$ . Therefore, by calculating  $a_{y_a}^{\text{IDP}}$  in accordance with the following equation:

$$a_{y_a}^{\text{IDP}} = \cos(\phi_c) a_{y_a}^e + \sin(\phi_c) a_{z_a}^e, \quad (3)$$

$y_a^{\text{IDP}}$  can be calculated as

$$y_a^{\text{IDP}} = y_{a0}^{\text{IDP}} + v_{y_{a0}}^{\text{IDP}} \cdot t + \iint a_{y_a}^{\text{IDP}}(t) dt^2, \quad (4)$$

where  $y_{a0}^{\text{IDP}}$  and  $v_{y_{a0}}^{\text{IDP}}$  are the initial position and velocity in  $y$  direction.

In the following two subsections, by exploiting the features of near-range SAR applications, two motion measuring algorithms are proposed, which use only low-cost MEMS IMU.

### 3.1. 1-DoF Algorithm

The synthetic aperture length of a certain target in near-range applications is much shorter than in remote sensing applications. For a short-term duration, when rotational motions of the vehicle are minor, it can be assumed that  $\omega_x = \omega_y = \omega_z = 0$ . In such a case, the calculation of  $a_y^{\text{IDP}}$  in (3) simplifies to

$$a_y^{\text{IDP}} = a_y^b + g \cdot \sin \phi_c, \quad (5)$$

and the subscript “ $a$ ” denoting antenna in (3) is omitted in the interest of brevity. Therefore it is possible to calculate  $y^{\text{IDP}}$  only using a one-axis accelerometer which measures  $a_y^b$ . The procedure of this 1-DoF algorithm for calculating  $y^{\text{IDP}}$  is shown in Figure 4.

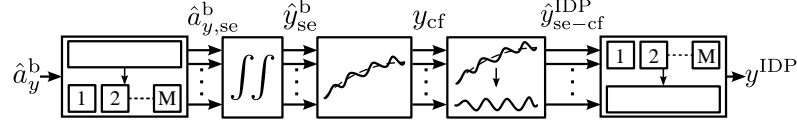


**Figure 4.** Procedure of 1-DoF motion measuring algorithm.

First, the sampled raw acceleration,  $\hat{a}_y^b$ , which contains bias drift and noise, is uniformly divided into  $M$  segments. The length of each segment,  $N_{se}$ , is determined by the performance of the accelerometer and the vehicle’s velocity [12]. Using (5), the raw acceleration in each segment,  $\hat{a}_{y,se}^b$ , can be written as

$$\hat{a}_{y,se}^b = a_y^{\text{IDP}} + (a_{\text{bias},y} - g \cdot \sin \phi_c) + n_{a_y}, \quad (6)$$

where  $a_{\text{bias},y}$  is the unknown device-specific bias of the accelerometer within each segment denoted with subscript “ $\text{bias}$ ”, and  $n_{a_y}$  is the overall noise of the accelerometer and ADC, which results in accumulated motion error.

After double integration, the trajectory of each segment can be obtained as

$$\hat{y}_{se}^b = \frac{1}{2} \left( a_{\text{bias},y}^b - g \sin \phi_c \right) t^2 + \iint a_y^{\text{IDP}} dt^2 + \iint n_{a_y} dt^2. \quad (7)$$

However, the expectation of the trajectory should be calculated as

$$y_{se}^{\text{IDP}} = y_0^{\text{IDP}} + v_{y_0}^{\text{IDP}} \cdot t + \iint a_y^{\text{IDP}} dt^2, \quad (8)$$

where  $y_0^{\text{IDP}}$  is the initial position and  $v_{y_0}^{\text{IDP}}$  is the initial velocity of each segment.

By performing a quadratic polynomial curve fitting on  $\hat{y}_{se}^b$ , the estimations of  $y_0^{\text{IDP}}$ ,  $v_{y_0}^{\text{IDP}}$  and  $\frac{1}{2} \left( a_{\text{bias},y}^b - g \cdot \sin \phi_c \right)$  can be obtained. The result of the curve fitting is a quadratic polynomial

$$y_{cf} = P_1 \cdot t^2 + P_2 \cdot t + P_3. \quad (9)$$

By subtracting (9) from (7), the estimation of  $y_{se}^{\text{IDP}}$  can be obtained as

$$\hat{y}_{se-cf}^{\text{IDP}} = -P_3 - P_2 \cdot t + \iint a_y^{\text{IDP}} dt^2 + \left[ \frac{1}{2} \left( a_{\text{bias},y}^b - g \cdot \sin \phi_c \right) - P_1 \right] t^2 + \iint n_{a_y} dt^2. \quad (10)$$

It can be seen that the device-specific  $a_{\text{bias},y}^b$ , which may change along temperature and time between segments, does not need to be measured. Moreover,  $P_1$  also compensates the quadratic component of the accumulated motion error  $\iint n_{a_y} dt^2$ . Therefore, the requirement for the accelerometer and the ADC can be considerably relaxed.

In the end, each  $\hat{y}_{se-cf}^{\text{IDP}}$  is connected to its adjacent segments to form the  $y^{\text{IDP}}$  for building the motion compensation phase term,  $e^{jk_r \Delta r_{\text{in}}}$ .

### 3.2. 3-DoF Algorithm

The rotation’s influence on the accelerometer measurements cannot be ignored beyond a certain level of rotational degrees. In order to cope with wider applications, where DCS varies over time in a three-dimensional space, a one-axis gyroscope is used to acquire  $\phi$  information. The procedure of the 3-DoF algorithm for calculating  $y^{\text{IDP}}$  is shown in Figure 5.

The acceleration  $a_y^b$  and  $a_z^b$  measured by the accelerometer and  $\phi$  calculated from the angular rate  $\omega_x$  measured by the gyroscope are used to calculate the acceleration  $a_y^{\text{IDP}}$  as follows

$$a_y^{\text{IDP}} = a_y^b \cos(\phi - \phi_c) - a_z^b \sin(\phi - \phi_c) + g \sin \phi_c. \quad (11)$$

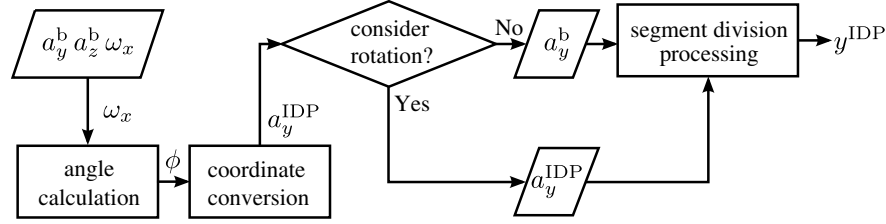


**Figure 5.** Procedure of 3-DoF motion measuring algorithm.

Note that (11) becomes (5) as used in the 1-DoF algorithm when  $\phi$  is constant and equal to its initial value  $\phi_c$ .

Then the decision, whether it is necessary to consider the influence of rotation, is made by calculating the ratio of the difference between rotation-including and rotation-ignoring  $a_y^{IDP}$  to rotation-ignoring  $a_y^{IDP}$  as

$$\left| \frac{a_y^b [\cos(\phi - \phi_c) - 1] - a_z^b \sin(\phi - \phi_c)}{a_y^b + g \sin \phi_c} \right| \gg 1. \quad (12)$$

From this point, the calculation continues to the same segment division processing as in 1-DoF algorithm. In the end the complete  $y^{IDP}$  is obtained by connecting the results of each segment.

#### 4. SETUP AND MEASUREMENTS

A SAR system has been built to verify the proposed motion measuring algorithms. As shown in Figure 6(a), the system contains an FMCW radar operating at 24 GHz, a rotary encoder attached on an auxiliary wheel for measuring the velocity, and a 6-DoF MEMS IMU board. The radar and motion sensors are mounted on the same board in order to be treated as a rigid body as shown in Figure 6(b). The rotary encoder is attached on an auxiliary wheel. When the magnetic actuator rotates with the wheel, the encoder body senses the rotation and generates an analog signal in proportional to the rotation angle. This output signal is synchronously sampled with the radar IF signal as well as other motion measurements, so the azimuth position of every IF samples can be known.

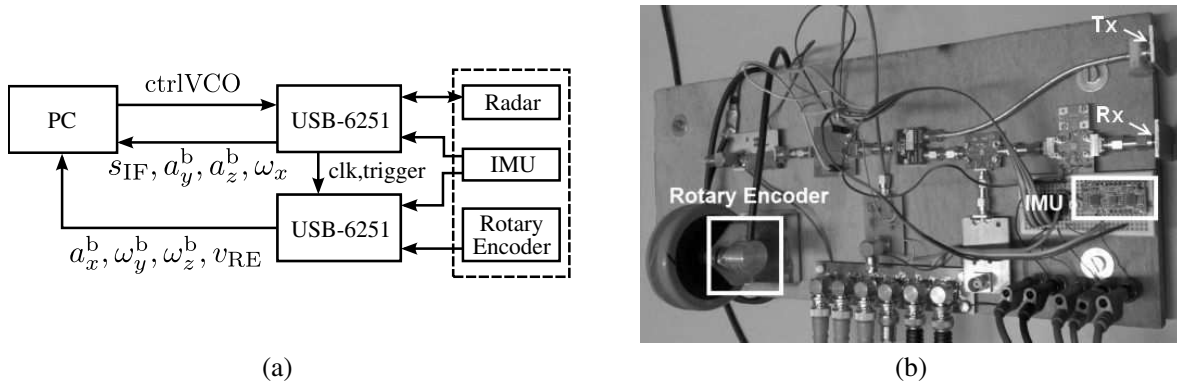


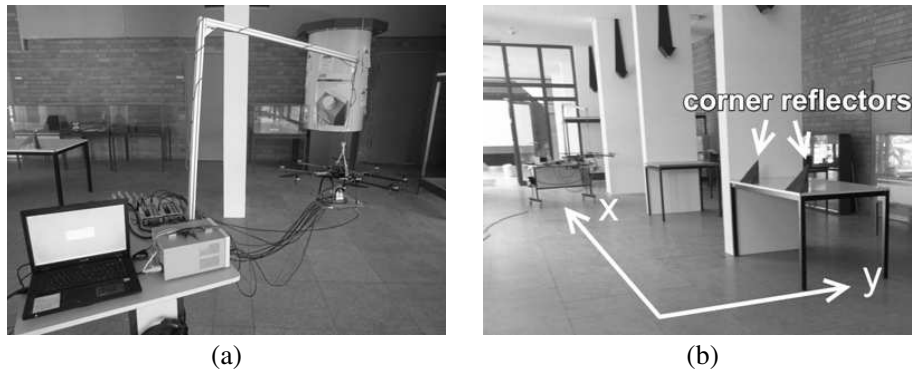
**Figure 6.** The FMCW SAR demonstrator. (a) Block diagram. (b) Photo of radar-motion-sensor board.

The measurements of radar and motion sensors are synchronously sampled by two data acquisition (DAQ) modules, NI USB-6251, which are controlled using LabView. The SAR processing and motion measuring algorithm are implemented using MATLAB and run in off-line mode. The 3-axis analog accelerometer on the IMU board is ADXL335. The angular rates,  $\omega_x$  and  $\omega_y$ , are measured by an analog gyroscope LPR530AL, and  $\omega_z$  is measured by an LY530ALH. The main parameters of the FMCW radar and the motion sensors are listed in Table 1.

**Table 1.** Parameters of radar and motion sensors.

Parameter	Description	Value
$f_{\min}$	Minimum frequency	23.5 GHz
$f_{\max}$	Maximum frequency	24.5 GHz
$\Psi$	Azimuth HPBW	33°
$\Phi$	Elevation HPBW	17°
$T_p$	Duration of chirp signal	application-specific
$\Delta r_{\text{ran}}$	Range resolution	15.0 cm
$\Delta r_{\text{azi}}$	Azimuth resolution (in SAR mode)	1.3 cm
$B_{\text{acc}}$	Bandwidth	50 Hz
$s_{\text{acc}}$	Sensitivity	300 mV/g
$N_{\text{acc}}$	Noise density	150 $\mu\text{g}/\sqrt{\text{Hz}}$
$B_{\text{gyr}}$	Bandwidth	50 Hz
$s_{\text{gyr}}$	Sensitivity (4x amplified)	3.33 mV/°/s
$N_{\text{gyr}}$	Noise density	0.035°/s/ $\sqrt{\text{Hz}}$
$\Delta\omega_{\text{bias}}$	Bias drift within a temperature range of 10°C	0.5°/s

The setup of MAV-borne SAR measurements is shown in Figure 7(a). Since the whole SAR system is too heavy to be carried by the MAV, only the radar-motion-sensor board was mounted under the landing support. The MAV was hanged on a metal arm which was fixed on a wheel-equipped table, and the other parts of the SAR system were put on the table. The SAR measurements were carried out by moving the table along the flying MAV to simulate a realistic flight campaign. The inherent vibrations of the MAV along with the maneuver were measured by the 6-DoF IMU board. As shown in Figure 7(b), the measurements were carried out in a hall. The scene consisted of several pillars, metal tables, a wall and two corner reflectors, which were approximately in the same height level with the radar’s trajectory.

**Figure 7.** Setup of MAV-borne SAR measurements. (a) Setup of system. (b) Geometry of measurements, where the system moved along the positive  $x$  axis (azimuth direction).

Within certain azimuth spans, motion errors are more severe than others and different between the 1-DoF and 3-DoF algorithms. Correspondingly, two regions, which are within these “severe” azimuth span and containing obvious targets, are selected to demonstrate the performance of proposed

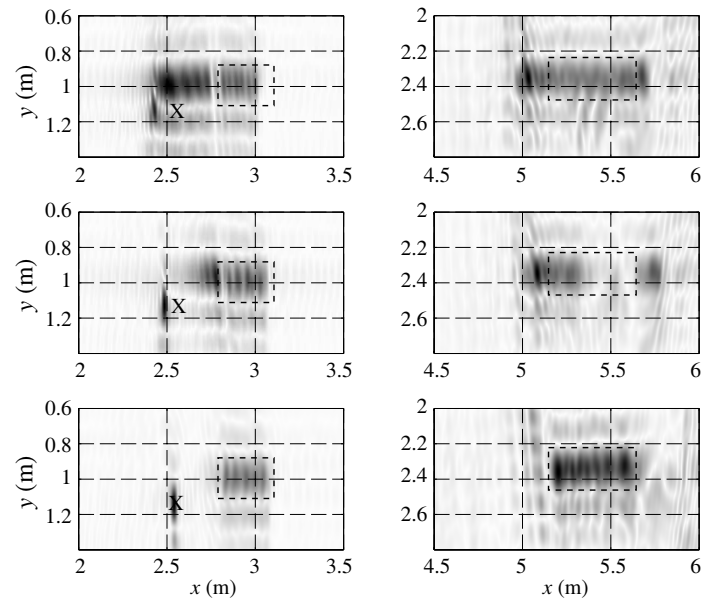


**Figure 8.** Normalized SAR images obtained from the MAV-borne SAR measurements (targets are denoted with “ $x$ ” and dash-line rectangles): Two regions are cropped from the same plots and shown in each column respectively; from up to down are results obtained without motion compensation, with 1-DoF and with 3-DoF motion measuring algorithms.

algorithms. In the left column of Figure 8, a corner reflector located at about (2.5, 1.1) m is denoted with “ $x$ ”; a pillar’s contour is denoted with a dash-line rectangle center at about (2.9, 1.0) m. It can be seen that, as a result of motion errors the image of the pillar is defocused and overlapped with the adjacent corner reflector. It is clear that, after motion compensation using both motion measuring algorithms, both targets are better refocused in the final SAR image. Since the motion errors deteriorated targets are not single point targets, it is difficult to give quantitative improvement comparison between the 1-DoF and 3-DoF algorithms. Nevertheless, it is obvious that the 3-DoF algorithm can measure the radar sensor’s trajectory more precisely than the 1-DoF algorithm, thereby resulting in better SAR image. Furthermore, the right column of Figure 8 shows a more severe case of motion errors. A metal table, whose contour is denoted with a dash-line rectangle center at about (5.4, 2.3) m, is imaged with the 3 different strategies. Here the 1-DoF algorithm wrongly measured the trajectory, thereby having worse result than the 3-DoF algorithm. Therefore, the 3-DoF algorithm should be applied when the rotation components in motion errors are beyond the tolerant level of the 1-DoF algorithm.

## 5. CONCLUSION

Two motion measuring algorithms using only low-cost MEMS IMU have been proposed. Due to the short-term-rotation-constant feature in the near-range SAR applications, not all 6 DoF are required to calculate the radar sensor’s trajectory. In addition, no external GPS signal is required, since the accumulated motion error caused by MEMS IMU’s high noises and biases is reduced via segment division processing. The algorithms have been verified by MAV-borne SAR measurements, which have been performed for the first time. The results show that the 3-DoF algorithm has better performance than the 1-DoF algorithm in high dynamics applications.

## ACKNOWLEDGMENT

The authors would like to thank the Institut fuer Theoretische Elektrotechnik und Systemoptimierung (ITE) of the Karlsruher Institut fuer Technologie (KIT), for supporting their project by supplying the MAV and assisting with the measurements.

**REFERENCES**

1. Meta, A., P. Hoogeboom, and L. P. Ligthart, "Signal processing for FMCW SAR," *IEEE Transactions on Geoscience and Remote Sensing*, Vol. 45, No. 11, 3519–3532, 2007.
2. IMSAR, "NanoSAR C data and specification sheet," 2013, [Online], Available: [http://www.imsar.com/uploads/files/46\\_NanoSAR\\_C\\_Data\\_Sheet.pdf](http://www.imsar.com/uploads/files/46_NanoSAR_C_Data_Sheet.pdf).
3. Roke Manor Research Limited, "Miniature radar altimeter MRA type 2," 2012, [Online], Available: <http://www.roke.co.uk/resources/datasheets/mra-type-2.pdf>.
4. Moses, A., M. J. Rutherford, and K. P. Valavanis, "Radar-based detection and identification for miniature air vehicles," *IEEE International Conference on Control Applications (CCA)*, 933–940, Sep. 2011.
5. Seibold, J., N. Frietsch, J. Gut, O. Meister, and G. Trommer, "Cooperative UAV-navigation-aiding based on UGV vision systems," *Symposium Gyro Technology*, Karlsruhe, Germany, 2010.
6. Weiss, S., M. W. Achtelik, S. Lynen, M. Chli, and R. Siegwart, "Real-time onboard visual-inertial state estimation and self-calibration of MAVs in unknown environments," *IEEE International Conference on Robotics and Automation (ICRA)*, 2012.
7. Ackerman, E., "Quadrotor + kinect = one weird looking robot," *IEEE Spectrum*, 2010, [Online], Available: <http://spectrum.ieee.org/automaton/robotics/diy/quadrotor-kinect-one-weird-looking-robot>.
8. Martinelli, A., "Vision and IMU data fusion: Closed-form solutions for attitude, speed, absolute scale, and bias determination," *IEEE Transactions on Robotics*, Vol. 28, No. 1, 44–60, 2012.
9. Cumming, I. G. and F. H. Wong, *Digital Processing of Synthetic Aperture Radar Data: Algorithms and Implementation*, Artech House, 2005.
10. Wu, H. and T. Zwick, "Octave division motion compensation algorithm for near-range wide-beam SAR applications," *Progress In Electromagnetics Research*, Vol. 144, 115–122, 2014.
11. Titterton, D. H. and J. L. Weston, *Strapdown Inertial Navigation Technology*, 2nd Edition, Institution of Electrical Engineers, 2004.
12. Wu, H. and T. Zwick, "A novel motion compensation method for automotive SAR: Simulations and experiments," *Proceedings of German Microwave Conference*, Berlin, Germany, 2010.